Supporting Information

$BaSbBS_4$: a record-high-performance birefringent crystal identified by a target-driven closed-loop strategy

Ming-Zhi Zhang[a,b], Yue Zhao[a], Chun-Li Hu*[a], Jiang-Gao Mao*[a,b]

a State Key Laboratory of Functional Crystals and Devices, Fujian Institute of Research on the Structure of Matter, Chinese Academy of Sciences, Fuzhou 350002 (P. R. China).
b University of Chinese Academy of Sciences, Beijing 100049 (P. R. China).
* Corresponding authors: mjg@fjirsm.ac.cn, clhu@fjirsm.ac.cn.

METHOD

1. Theoretical methods

1.1 A deep learning model for precise band gap prediction

It is well-known that the optical property simulation of crystals is intrinsically dependent on precise band gap data. However, conventional DFT calculations using the generalized gradient approximation (GGA) with the Perdew-Burke-Ernzerhof (PBE) functional tend to greatly underestimate the band gaps of compounds, and therefore more accurate hybrid functional methods, such as the Heyd-Scuseria-Ernzerhof (HSE), are highly required, but they are extremely time-consuming.

Emerging as the most promising methodology for data-driven function approximation, machine learning (ML) has been employed to predict the band gaps of crystalline solids, that is facilitated by the substantial growth of open-access databases. However, due to the limited experimental band gap data, previous ML models, such as the Crystal Graph Convolutional Neural Networks (CGCNN)[1], MatErials Graph Network (MEGNet)[2] and SchNet[3], were typically trained on large datasets computed by DFT-PBE. Consequently, such models passively inherit the underlying discrepancies between DFT computations and experimental observations, in addition to the prediction error with respect to DFT computations used for training.

In this work, based on a high-quality dataset comprising 10,481 materials with HSE-level computed band gaps from the SNUMAT database[4], we employed a transfer learning approach to fine-tune the parameters of a pretrained MatErials Graph Network (MEGNet) model and developed a new deep learning model to predict the band gaps of crystals at the HSE level. The details of the dataset and the train settings of the deep learning model are as follows.

1.1.1 Dataset

The dataset plays a pivotal role in machine learning technology because it is

mandatory to use a large number of high-quality data to achieve robust and accurate prediction. In this study, to train and test the ML regression model, the SNUMAT database which contains the band gaps for 10481 materials calculated at the HSE level is utilized[4]. These materials comprise 63 unitary, 1,919 binary, 5,074 ternary, 2,804 quaternary, 573 quinary, and 48 higher-order compounds sourced from Inorganic Crystal Structure Database (ICSD) and Materials Project (MP). The dataset is validated against the experimental data and shows good quality. For model development, the data were then randomly split into 80% (8380) for training, 10% (1047) for validation, and 10% (1048) for testing, with this process repeated six times to ensure reliability.

1.1.2 Train settings of the deep learning model

We utilized a pre-trained MEGNet model for GGA-PBE-based band gap prediction as the initial model. This initial model was trained on a big dataset of 45901 crystals with a finite band gap from the Materials Project [5] obtained via the Python Materials Genomics (*pymatgen*) [6] interface to the Materials Application Programming Interface (API) [7] on June 1, 2018, and it outperforms prior state-of-the-art models, such as the SchNet [3] and CGCNN [1] models, in the PBE-based band gap prediction. The model architecture is detailed in Table S1. We only frozen the pre-training weights of the embedding layer, which encode useful chemical information that can be transferred learned to develop models with better convergence and lower errors [2], and the weights of the other layers (including MEGNet and Dense layers) were fine-tuned on the above HSE-based bandgap datasets. The new model was trained for 1000 epochs with a learning rate of 0.0001 and a minibatch size of 32 by utilizing the Adam optimizer.

For evaluation, both mean absolute error (MAE) and coefficient of determination (R^2) were calculated to quantify the deviation between the predicted and true values, as expressed by the following formulas:

$$MAE = \frac{1}{n}\sum_{i=1}^{n}\left|\hat{y}_i - y_i\right|$$

$$R^2 = 1 - \frac{\sum_{i=1}^{n} (\hat{y}_i - y_i)^2}{\sum_{i=1}^{n} (y_i - \bar{y}_i)^2}$$

where the yi denotes the true property value and y_i represents the model's prediction.

As shown in Figure S1a, the deep learning model shows excellent prediction accuracy with a low MAE (0.1205 eV) in the test subset. As for R^2, the value of 0.9763 (close to 1) also indicates good fitting capability of the model on the test data. Notably, the MAE and R^2 in the training and validation subsets are close to those of the test subset (Figure S1b and S1c), indicating that the model is not overfitted and has a good generalization ability.

1.2 High-throughput DFT computation

All the DFT calculations were performed based on their single crystal structures data. The electronic structures and optical properties were calculated based on the plane wave pseudopotential method implemented in the total energy code CASTEP. [8] [9] For the exchange and correlation function, we chose Perdew-Burke-Ernzerhof (PBE) in the generalized Gradient Approximation (GGA) [10]. The interactions between ionic cores and electrons were described by the norm-conserving pseudopotential [11]. The following valence-electron configurations were considered in the computation: Ba $5s^2 5p^6 5d^{10} 6s^2$, B $2s^2 2p^1$, Sb $5s^2 5p^3$, S $3s^2 3p^4$ for $BaSbBS_4$. The number of plane waves included in the basis sets was determined by cutoff energy of 650 eV. The Monkhorst-Pack k-point separation was set to 0.04 $Å^{-1}$ to perform numerical integration of the Brillouin zone. During the optical property calculations, the number of empty bands was set to two times that of valence bands to ensure the convergence of dielectric functions and refractive indices.

The calculations of linear optical properties in terms of the complex dielectric function $\boldsymbol{\varepsilon(\omega) = \varepsilon_1(\omega) + i\varepsilon_2(\omega)}$ were made. The imaginary part $\boldsymbol{\varepsilon_2(\omega)}$ can be used to describe the real transitions between occupied and unoccupied electronic states, which

was given in the following equation [12],

$$\varepsilon_2^{ij}(\omega) = \frac{8\pi^2\hbar^2e^2}{m^2V}\sum_k\sum_{cv}(f_c - f_v)\frac{p_{cv}^{i}(k)p_{vc}^{j}(k)}{E_{vc}^2}\delta[E_c(k) - E_v(k) - \hbar\omega]$$

The f_c and f_v represent the Fermi distribution functions of the conduction and valence bands, respectively. The term $p_{cv}^{i}(k)$ denotes the momentum matrix element transition from the energy level *c* of the conduction band to the level *v* of the valence band at a certain *k* point in the Brillouin zones and ***V*** is the volume of the unit cell. The ***m***, ***e*** and ***ħ*** are the electron mass, charge and Plank's constant, respectively.

Since the dielectric function describes a causal response, the real part $\varepsilon_1(\omega)$ can be obtained via Kramer-Kronig transform. All optical constants will be derived from the dielectric function $\varepsilon(\omega)$, and our main concern, the refractive index $n(\omega)$ can be expressed as

$$n(\omega) = (1/\sqrt{2})[\sqrt{\varepsilon_1(\omega)^2 + \varepsilon_2(\omega)^2} + \varepsilon_1(\omega)]^{1/2}$$

Based on the above theory and methods, we have created a high-throughput computation platform for crystal optics, which can realize batch computation, automatic analysis and data extraction of electronic structures and optical properties of crystals. It provides a guarantee for the efficient calculations and analyses of the birefringent properties of a large number of crystals.

1.3 Polarizability anisotropy-weighted electron density

To reveal the electronic and structural origin of birefringence, we defined polarizability anisotropy-weighted electron density [PAWED, $\rho_{\Delta\chi}(r)$] [13]. It contains two parts of contributions (from VB and CB) and can be formulized as：

$$\rho_{\Delta\chi}^{VB}(r) = \sum_i^{VB}\omega_i|\psi_i(r)|^2$$

$$\rho_{\Delta\chi}^{CB}(r) = \sum_i^{CB}\omega_i|\psi_i(r)|^2$$

where $|\psi_i(r)|^2$ is the electron density of the *i*th band/orbital; ω_i is the weighting

factor, which describes the contribution ratio of the *i*th band/orbital to total polarizability anisotropy ($\Delta\chi^{(1)}$) of a crystal. In the low-frequency region, ω_i can finally be quantified by dielectric function ε,

$$\omega_i = \frac{\Delta\chi_i^{(1)}}{\Delta\chi^{(1)}} = \frac{\varepsilon_i(\alpha\alpha) - \varepsilon_i(\beta\beta)}{\varepsilon(\alpha\alpha) - \varepsilon(\beta\beta)}$$

And utilizing PAWED technique, the orbital contributions to the birefringence (optical anisotropy) can be shown visually, and the groups/ions' contributions can further be identified.

2. Experimental methods

2.1 Synthesis

The start materials are BaS (99.999% Beijing Hawk Science), Sb_2S_3(98%, Shanghai Aladdin Biochemistry Technology), amorphous B powder (99.9%, Shanghai Aladdin Biochemistry Technology), S Powder (98%, Shanghai Aladdin Biochemistry Technology).

The mixture of BaS, Sb_2S_3, B, S with a molar ratio of 1:1:1:4 was grinded into fine powder, and then was transferred to a graphite crucible which is used to avoid the reaction between B and SiO_2. Then the crucible was sealed into a quartz tube under a vacuum of 10^{-2} Pa. Then the quartz tube was placed into a muffle furnace and heated to 850 ℃ within 24 h, held for 72 h, then slowly cooled down to room temperature in 200 h. The product was washed by anhydrous ethanol. Orange-yellow needle-like single crystals were collected in a yield of about 60%. These crystals are not sensitive to moisture and are air stable for serval months.

2.2 Single Crystal X-ray Diffraction

Single-crystal X-ray diffraction data for $BaSbBS_4$ was collected using an Agilent SuperNova dual-wavelength CCD diffractometer with Mo K_α radiation (λ = 0.71073Å). The CrysAlisPro software package was utilized for data reduction. Numerical absorption corrections based on Gaussian integration over a multifaceted crystal model and empirical absorption corrections using spherical harmonics implemented in SCALE3 ABSPACK scaling algorithm were applied [14]. The structures were solved by direct methods and refined using full-matrix least-squares fitting on F^2 with SHELXL-

2017 [15]. PLATON [16] was used for checking possible missing symmetry elements and none was found. Crystal data were listed in table S3.

2.3 Powder X-ray Diffraction

Powder x-ray diffraction data were collected via Rigaku MiniFlex600 diffractometer. Scanning was performed with a scan step width of 0.02° using Cu Kα radiation (λ = 1.541886 Å) in the 2θ range of 10 – 70°.

2.4 Energy-Dispersive X-ray Spectroscopy

Elemental analyses were carried out using a field-emission scanning electron microscope (JSM6700F) outfitted with an Oxford INCA energy-dispersive X-ray spectroscope.

2.5 Infrared Spectrum

IR spectra were recorded on A Nicolet Magna 750 Fourier Transform Infrared spectrometer in the spectral range of 4000 to 400 cm^{-1}.

2.6 Thermogravimetric analysis (TGA)

TGA was measured on a NETZCH STA 449F3 thermal analyzer and sample powders were heated under N_2 gas atmosphere from room temperature to 1000 °C at a rate of 10 °C /min.

2.7 Birefringence

The birefringence was studied on a polarizing microscope (ZEISS Axio Scope. A1) equipped with a tilting compensator.

2.8 UV-Vis-NIR diffuse reflectance spectroscopy

The ultraviolet-visible-near-IR (UV-Vis-NIR) diffuse reflectance spectrum in the range of 200-2000 nm was collected using a PerkinElmer Lambda 950 UV-Vis-NIR spectrophotometer, with a barium sulfate powder plate as a 100% reflectance reference. Absorption data is converted from the reflection data by the Kubelka - Munk function

α/S = (1 − R)2/2R (α is the absorption coefficient, S the scattering coefficient, and R the reflectance. The band gap value is the abscissa of the intersection of the absorption edge extension line and the zero absorption.

Table S1. The architecture of the pre-trained MEGNet model.

Layer (type)	Output Shape	Param#	Connected to
input_1 (InputLayer)	[(None, None)]	0	[]
embedding_1 (Embedding)	(None, None, 16)	1520	['input_1[0][0]']
input_2 (InputLayer)	[(None, None, 100)]	0	[]
input_3 (InputLayer)	[(None, None, 2)]	0	[]
dense_1 (Dense)	(None, None, 64)	1088	['embedding_1[0][0]']
dense_3 (Dense)	(None, None, 64)	6464	['input_2[0][0]']
dense_5 (Dense)	(None, None, 64)	192	['input_3[0][0]']
dense_2 (Dense)	(None, None, 32)	2080	['dense_1[0][0]']
dense_4 (Dense)	(None, None, 32)	2080	['dense_3[0][0]']
dense_6 (Dense)	(None, None, 32)	2080	['dense_5[0][0]']
input_4 (InputLayer)	[(None, None)]	0	[]
input_5 (InputLayer)	[(None, None)]	0	[]
input_6 (InputLayer)	[(None, None)]	0	[]
input_7 (InputLayer)	[(None, None)]	0	[]

meg_net_layer_1 (MEGNetLayer)	[(None, None, 32), (None, None, 32), (1, None, 32)]	39392	['dense_2[0][0]', 'dense_4[0][0]', 'dense_6[0][0]', 'input_4[0][0]', 'input_5[0][0]', 'input_6[0][0]', 'input_7[0][0]']
add_1 (Add)	(None, None, 32)	0	['dense_2[0][0]', 'meg_net_layer_1[0][0]']
add_2(Add)	(None, None, 32)	0	['dense_4[0][0]', 'meg_net_layer_1[0][0]']
add_3 (Add)	(None, None, 32)	0	['dense_6[0][0]', 'meg_net_layer_1[0][0]']
dense_7 (Dense)	(None, None, 64)	2112	['add_1[0][0]']
dense_9 (Dense)	(None, None, 64)	2112	['add_2[0][0]']
dense_11 (Dense)	(None, None, 64)	2112	['add_3[0][0]']
dense_8 (Dense)	(None, None, 32)	2080	['dense_7[0][0]']
dense_10 (Dense)	(None, None, 32)	2080	['dense_9[0][0]']
dense_12 (Dense)	(None, None, 32)	2080	['dense_11[0][0]']
meg_net_layer_2 (MEGNetLayer)	[(None, None, 32), (None, None, 32), (1, None, 32)]	39392	['dense_8[0][0]', 'dense_10[0][0]', 'dense_12[0][0]', 'input_4[0][0]', 'input_5[0][0]', 'input_6[0][0]', 'input_7[0][0]']
add_4 (Add)	(None, None, 32)	0	['add_1[0][0]', 'meg_net_layer_2[0][0]']
add_5 (Add)	(None, None, 32)	0	['add_2[0][0]', 'meg_net_layer_2[0][0]']
add_6 (Add)	(None, None, 32)	0	['add_3[0][0]', 'meg_net_layer_2[0][0]']
dense_13 (Dense)	(None, None, 64)	2112	['add_4[0][0]']
dense_15 (Dense)	(None, None, 64)	2112	['add_5[0][0]']
dense_17 (Dense)	(None, None, 64)	2112	['add_6[0][0]']

dense_14 (Dense)	(None, None, 32)	2080	['dense_13[0][0]']
dense_16 (Dense)	(None, None, 32)	2080	['dense_15[0][0]']
dense_18 (Dense)	(None, None, 32)	2080	['dense_17[0][0]']
meg_net_layer_3 (MEGNetLayer)	[(None, None, 32), (None, None, 32), (1, None, 32)]	39392	['dense_14[0][0]', 'dense_16[0][0]', 'dense_18[0][0]', 'input_4[0][0]', 'input_5[0][0]', 'input_6[0][0]', 'input_7[0][0]']
add_7 (Add)	(None, None, 32)	0	['add_4[0][0]', 'meg_net_layer_3[0][0]']
add_8 (Add)	(None, None, 32)	0	['add_5[0][0]', 'meg_net_layer_3[0][0]']
set2_set_1 (Set2Set)	(None, None, 32)	2640	['add_7[0][0]', 'input_6[0][0]']
set2_set_2(Set2Set)	(None, None, 32)	2640	['add_8[0][0]', 'input_7[0][0]']
add_9 (Add)	(None, None, 32)	0	['add_6[0][0]', 'meg_net_layer_3[0][2]']
concatenate_1 (Concatenate)	(None, None, 96)	0	['set2_set_1[0][0]', 'set2_set_2[0][0]', 'add_9[0][0]']
dense_19 (Dense)	(None, None, 32)	3104	['concatenate_1[0][0]']
dense_20 (Dense)	(None, None, 16)	528	['dense_19[0][0]']
dense_21 (Dense)	(None, None, 1)	17	['dense_20[0][0]']

Table S2. ML-predicted or experimental band gaps and calculated birefringence of compounds by statistic.

Unit	Compound	*E*g（experimental*/ML-predicted）	space group	Δn_{cal} 546nm	Δn_{cal} 1064nm	Ref.
AsS_3	Ag_3AsS_3(*R*3*c*)	2.00*/2.31	*R*3*c*	0.237	0.331	17
	Ag_3AsS_3(*C*2/*c*)	2.37	*C*2/*c*	0.311	0.197	18
	$BaCd_2As_2S_6$	2.60* / 2.33	*Cmca*	0.169	0.129	19
	$BaHg_2As_2S_6$	2.47	*Cmca*	0.130	0.134	
	$K_2SnAs_2S_6$	2.23	*P*-3	0.574	0.387	20
	As_2S_3 (*P*2$_1$/*n*)	2.67	*P*2$_1$/*n*	0.509	0.414	21
	As_2S_3 (*P*-1)	2.59	*P*-1	0.254	0.202	22
	β-As_4S_3	2.54	*Pnma*	0.076	0.075	23
	α- As_4S_3	2.50	*Pnma*	0.063	0.064	
	As_4S_5	2.59	*P*2$_1$/*m*	0.192	0.147	24
	As_8S_9	2.57	*P*2/*c*	0.032	0.007	25
	As_4S_3(CuCl)	2.59	*Pbcm*	0.233	0.181	26
	$As_4S_3(CuCl)_2$	2.56	*P*2$_1$/*m*	0.302	0.202	
	$AgHgAsS_3$	1.94	*Cc*	0.279	0.198	27
	$AsPS_4$	2.70* / 2.72	*P*-1	0.268	0.198	28
	$Ba_2As_2S_5$	2.02* / 2.54	*Pca*2$_1$	0.187	0.144	29
	Ba_2AsS_3Br	2.80* / 3.13	*Pnma*	0.178	0.135	30
	Ba_2AsS_3Cl	2.80* / 3.19	*Pnma*	0.187	0.142	
	Ba_2AsS_3I	2.80* / 3.12	*Pnma*	0.180	0.132	
	$Cs_2As_8S_{13}$	2.31	*Pbcn*	0.566	0.404	31
	$CsHgAsS_3$	2.64* / 2.75	*P*2$_1$/*n*	0.220	0.160	32
	$Cs_3AgAs_4S_8$	2.24* / 2.60	*C*2/*c*	0.097	0.060	33
	$Cs_2Ag_2As_2S_5$	2.48* / 2.69	P-1	0.247	0.160	
	$Cs_3CuAs_4S_8$	2.26* / 2.66	*C*2/*c*	0.184	0.107	34
	$CsCu_2AsS_3$	2.26* / 2.11	*Pbca*	0.493	0.319	35
	$CsAg_2AsS_3$	2.70* / 2.84	*P*2$_1$/*c*	0.200	0.137	36
	$Cu_{12}(As_3S_7)(As_5S_{11})$	1.03	*P*1	0.074	0.140	37
	Hg_3AsS_4Br	2.18	*P*6$_3$*mc*	0.508	0.390	38
	Hg_3AsS_4Cl	2.43	*P*6$_3$*mc*	0.516	0.383	
	KAg_2AsS_3	2.25* / 2.48	*P*-1	0.336	0.234	39
	KCu_2AsS_3	1.78	*P*-1	0.459	0.361	40
	$La_3(AsS_3)S_2Cl_2$	3.09	*Cc*	0.059	0.032	-

	Li_3AsS_3	3.20	$Pna2_1$	0.297	0.252	[41]
	$LiAsS_2$	1.60* / 1.38	Cc	0.536	0.590	[42]
	$NaAsS_2$	2.23* / 2.46	$P2_1/b$	0.628	0.372	
	$NaCdAsS_3$	2.93* / 2.63	$P2_1/n$	0.034	0.020	[43]
	$Pb_4As_2S_6ICl$	2.48	$Pmn2_1$	0.299	0.206	[44]
	$Pb_2As_2S_5$	1.72	$P2_1$	0.340	0.276	[45]
	$PbAgAsS_3$	2.16	$P2_1/a$	0.156	0.122	[46]
	$Rb_8Cu_6As_8S_{19}$	1.80* / 2.29	$P2_1$	0.101	0.068	[47]
	$RbAg_2AsS_3$	2.30* / 2.46	P-1	0.323	0.224	[48]
	$RbCu_2AsS_3$	1.96* / 2.23	$P2_1$/c	0.277	0.236	[49]
SbS_3	Ag_3SbS_3($P2_1/n$)	2.06	$P2_1/n$	0.105	0.091	[50]
	Ag_3SbS_3($R3c$)	2.03	$R3c$	0.242	0.153	[51]
	Ag_3SbS_3($P2_1/c$)	2.03	$P2_1/c$	0.080	0.074	[52]
	$Ba_3Sb_2S_7$	2.52	$C2/c$	0.138	0.087	[53]
	Ba_2AlSbS_5	2.57* / 3.04	$Pnma$	0.241	0.137	[54]
	$Ba_2Sb_4GeS_{10}$	2.08	$P4_2/mbc$	0.225	0.158	[55]
	Ba_2SbS_3I	2.64* / 2.99	$Pnma$	0.195	0.131	[30]
	$BaAgSbS_3$	2.20* / 2.20	$C2/c$	0.263	0.191	[56]
	$BaSb_2S_4$	1.82	$P2_1/c$	0.605	0.481	[57]
	$Ba_8Sb_6S_{17}$	2.06	$P2/c$	0.051	0.079	[58]
	$Ca_2Sb_2S_5$	1.76	$P2_1/c$	0.434	0.286	-
	$CdSbS_2Br$	2.0* / 2.41	$C2/m$	0.655	0.382	[59]
	$CdSbS_2Cl$	2.2* / 2.45	$Pnma$	0.677	0.418	
	$CdSb_6S_8I_4$	2.11	P-1	0.514	0.338	-
	$Cs_2HgSb_4S_8$	2.13* / 2.48	P-1	0.185	0.099	[60]
	$Cs_2Sb_2(Sn_3S_{10})$	2.34* / 2.46	$P2_1/n$	0.140	0.106	[61]
	$Cs_2Sb_4S_7$	2.27	$P2_1/c$	0.708	0.479	[62]
	$Cs_2ZnSb_2S_5$	2.16* / 2.85	$C2/c$	0.417	0.261	[63]
	$Cs_4Sb_4S_8$	2.11* / 2.97	$Pnma$	0.433	0.292	[64]
	$CsSb_5S_8$	1.87* / 1.85	$P2_1/n$	0.789	0.501	[65]
	$CsSbS_2$	2.62	$P2_1/c$	0.469	0.283	-
	$Cs_2Cu_2Sb_2S_5$	1.60* / 2.10	P-1	0.490	0.431	[47]
	$Cs_2Ag_3Sb_3S_7$	2.02* / 2.27	$Cmc2_1$	0.352	0.213	[66]
	$CsAg_2SbS_3$	2.05* / 2.36	P-1	0.337	0.246	[48]
	$CsAgSb_4S_7$	2.04* / 2.19	$C2/c$	0.689	0.437	[67]
	$Cs_2Ba_3Cu_2Sb_2S_{10}$	1.98* / 2.25	$C2/m$	0.441	0.264	[68]
	$Cu_6Hg_3Sb_4S_{12}$	1.09	$R3$	0.045	0.216	[69]

	$CuSbS_2$	1.50* / 1.42	*Pnma*	0.503	0.421	[70]
	Hg_3SbAsS_3	1.95	$P2_1/n$	0.238	0.156	[71]
	$InSb_2S_4Br$	1.80* / 2.20	$C2/m$	1.253	0.903	[72]
	$InSb_2S_4Cl$	1.80* / 2.20	$C2/m$	1.340	0.982	
	$K_2Sb_2(Sn_3S_{10})$	2.30* / 2.31	$P2_1/n$	0.161	0.122	[61]
	$KHgSbS_3$	2.28	$C2/c$	0.223	0.154	[73]
	KSb_5S_8	1.61* / 1.59	*Pc*	0.385	0.483	[65]
	KCu_2SbS_3	1.70* / 1.78	*P*-1	0.428	0.390	[74]
	$K_2Ba_3Cu_2Sb_2S_{10}$	1.90* / 2.30	$C2/m$	0.453	0.259	[68]
	KAg_2SbS_3	2.10* / 2.27	*P*-1	0.335	0.239	[75]
	$La_3SbS_5Cl_2$	2.31* / 2.64	*Cc*	0.084	0.037	[76]
	$La_5Sb_2S_9Cl_3$	2.60* / 2.66	*Pbcm*	0.052	0.016	
	$La_8Sb_2S_{15}$	2.30* / 2.09	$I4_1cd$	0.034	0.019	[77]
	$LaSbS_2Br_2$	2.72* / 2.90	$P2_1/c$	0.102	0.078	[78]
	La_2CuSbS_5	2.06* / 2.30	*Ima*2	0.265	0.134	[79]
	$Li_3Sb_{11}S_{18}$	2.18	*P*-1	0.501	0.362	[80]
	Li_3SbS_3	3.02	$Pna2_1$	0.282	0.222	[41]
	$LiSrSbS_3$	2.30* / 2.79	$P2_1/c$	0.359	0.215	[81]
	$LiBaSbS_3$	2.23* / 3.02	*Pbam*	0.070	0.044	[82]
	$NaBaSbS_3$	2.46* / 2.65	$P2_1/c$	0.218	0.172	
	$NaCdSbS_3$	2.03	$C2/c$	0.221	0.236	[43]
	Na_2CuSbS_3	2.01	$P2_1/n$	0.461	0.371	[83]
	α-$NaSbP_2S_6$	2.17* / 2.77	$P2_1/c$	0.232	0.086	[84]
	β-$NaSbP_2S_6$	2.25* / 2.76	$P2_1$	0.129	0.058	
	$Rb_2Sb_2(Sn_3S_{10})$	2.33* / 2.41	$P2_1/n$	0.146	0.107	[61]
	$Rb_2Sb_4S_7$($P2_1/c$)	1.73*/2.03	$P2_1/c$	0.654	0.611	[85]
	$Rb_2Sb_4S_7$(*P*-1)	2.03	*P*-1	0.200	0.174	-
	$Rb_2ZnSb_4S_8$	1.88* / 2.48	*P*1	0.243	0.143	[86]
	$RbSb_5S_8$	1.60* / 1.65	*Pc*	0.387	0.480	[65]
	$Rb_2HgSb_4S_8$	1.82* / 2.35	*P*-1	0.211	0.130	[86]
	$Rb_2Cu_2Sb_2S_5$	1.60* / 2.06	$P2_1/c$	0.425	0.392	[47]
	$Rb_2Ba_3Cu_2Sb_2S_{10}$	1.93* / 2.27	$C2/m$	0.450	0.263	[68]
	$Rb_2Ag_3Sb_3S_7$	2.11* / 2.18	$Cmc2_1$	0.354	0.213	[66]
	Sb_2S_3	1.95* / 1.75	*Pbnm*	1.189	0.685	[87]
	$Sr_3Sb_4S_9$	1.34	$Pna2_1$	0.913	1.446	-
	$PbCuSbS_3$	1.42	$Pn2_1m$	0.598	0.271	[88]

	$Sr_6Sb_6S_{17}$	1.92* / 2.12	$P2_12_12_1$	0.687	0.507	[89]
SnS_3	$Ag_4SnGe_2S_7$	2.40* / 1.97	*Cc*	0.034	0.010	[90]
	$BaSn_2S_3$	1.78	$P2_1/c$	0.313	0.171	[91]
	$BaSnS_2$	2.40*/1.98	$P2_1$/c	0.381	0.226	[92]
	$Sn(SnS_3)$	1.43	*Pnma*	0.181	0.119	[93]
	$Sn_2Ga_2S_5$	2.02* / 2.01	$Pna2_1$	0.172	0.166	[94]
	Sn_2SiS_4	2.00* / 2.45	$P2_1/c$	0.192	0.186	[95]
	$Sn_2Sb_2S_5$	0.90	*Pnma*	1.058	1.079	[96]
	SnS (Pnma)	1.32* / 1.21	*Pnma*	1.312	1.148	[97]
BiS_3	$CuBiS_2$	1.13	Pnma	0.267	0.233	[98]
	Cu_3BiS_3	1.53	$P2_12_12_1$	0.081	0.101	[99]
BS_3	$Ba_3BS_3PS_4$	3.40* / 3.18	*Pnma*	0.124	0.110	[100]
	B_8S_{16}	3.68	$P2_1/c$	0.529	0.464	[101]
	$Ba_7(BS_3)_4S$	3.19	*C*2/*c*	0.071	0.065	[102]
	BaB_2S_4	3.55* / 3.45	*Cc*	0.040	0.026	[103]
	Cs_3BS_3	3.63	$P2_1/c$	0.046	0.038	[104]
	HgB_2S_4	3.36* / 3.20	$P2_1/n$	0.456	0.385	[105]
	$K_3(B_3S_6)$	3.71	*R*-3*cH*	0.455	0.388	[106]
	K_3BS_3	3.68	$P2_1/c$	0.060	0.051	[107]
	$LaBS_3$	2.9* / 2.61	$Pna2_1$	0.169	0.142	[108]
	Li_2CsBS_3	3.59	*Pnma*	0.187	0.152	[104]
	Li_3BS_3	3.29	*Pnma*	0.307	0.252	[109]
	$LiBaB_3S_6$	3.78	*Cc*	0.437	0.372	[110]
	$LiBaBS_3$ ($P2_1/c$)	3.45	$P2_1/c$	0.161	0.141	
	$LiBaBS_3$(*Pnma*)	3.23	*Pnma*	0.246	0.212	[111]
	$LiSr(B_3S_6)$	3.74	*Cc*	0.461	0.389	[106]
	$LiSrBS_3$	3.69	*Pnma*	0.175	0.148	[112]
	Na_3BS_3	3.62	*C*2/*c*	0.187	0.162	[107]
	$NaBaBS_3$	3.96* / 3.33	$P2_1/c$	0.167	0.147	[111]
	$Rb_3(B_3S_6)$	3.82	*R*-3*cH*	0.425	0.364	[106]
	Rb_3BS_3	3.66	$P2_1/c$	0.047	0.039	[107]
	$Sr_3(BS_3)_2$	3.36	*C*2/*c*	0.126	0.110	[113]
	$Sr_3(B_3S_6)_2$	3.67	*R*-3*H*	0.529	0.440	
	$Sr_3RbB_2S_6Br$	3.70* / 3.40	$Cmc2_1$	0.139	0.160	[114]
	$Sr_3RbB_2S_6Cl$	3.64* / 3.55	*Pbca*	0.155	0.136	
	$Na_3B_3S_6$	3.49	*R*-3*cH*	0.496	0.416	[106]
	$Na_2B_2S_5$	3.59	*Pnma*	0.541	0.475	[115]

combination	$Ba_6(BS_3)_3(BiS_3)$	2.43* / 2.53	$P2_1/c$	0.159	0.122	[116]
	$Ba_6(BS_3)_3(SbS_3)$	3.01* / 2.87	$P2_1/c$	0.157	0.130	
	$Ba_{13}(BS_3)_6(SnS_6)$	2.69* / 2.78	*R*-3	0.264	0.189	[117]
	$BaBiBS_4$	2.34* / 2.71	*Pnma*	0.696	0.386	[118]
	Ba_3BSbS_6	2.62* / 3.12	*P*-6	0.035	0.039	[116]
	$PbSbBS_4$	1.75* / 2.55	$P2_1/m$	1.059	0.620	[119]
	$PbBiBS_4$	2.51	$P2_1/m$	0.802	0.465	[119]
	$BaSbBS_4$	2.70* / 3.05	*Pnma*	0.943	0.566	[118]

Table S3. Summary of Crystallographic data and structure refinement parameters for $BaSbBS_4$.

Formula	$BaSbBS_4$
formula weight	398.14
temperature (K)	296.15
crystal system	Orthorhombic
space group	*Pnma*
a (Å)	9.6601(12)
b (Å)	6.2154(7)
c (Å)	11.6330(13)
V (Å^3)	698.46(14)
Z	4
ρ_{calc} (g/cm^3)	3.786
μ (mm^{-1})	10.540
F(000)	704.0
λ (Mo Kα) (Å)	0.71073
Rint	0.0653
Goodness-of-fit on F^2	1.078
R1, wR2 [I>2σ (I)][a]	0.0342, 0.0779
R1, wR2 (all data)	0.0430, 0.0845

[a]$R_1 = \Sigma||F_o|-|F_c||/\Sigma|F_o|$ and $wR_2 = \{\Sigma[w(F_o^2-F_c^2)^2]/\Sigma[w(F_o^2)^2]\}^{1/2}$.

Table S4. Atomic coordinates ($\times 10^4$) and equivalent isotropic displacement parameters ($Å^2 \times 10^3$) for $BaSbBS_4$. U_{eq} is defined as 1/3 of the trace of the orthogonalized UIJ tensor.

Compounds	Atom	*x*	*y*	*z*	U(eq)
$BaSbBS_4$	Ba(1)	4862.3(5)	2500	3309.4(4)	17.48(16)
	Sb(1)	1890.6(6)	7500	4597.9(4)	16.69(17)
	S(3)	4268(2)	7500	4076.7(17)	17.6(4)
	S(2)	2068.3(15)	4986(2)	6290.9(12)	17.6(3)
	S(1)	1700(2)	2500	3980.9(18)	21.4(4)
	B(1)	1918(9)	2500	5480(7)	12.7(17)

Table S5. Selected bond distances (Å), bond angles and calculated BVS for $BaSbBS_4$.

$BaSbBS_4$			
Bond		**length**	**BVS**
Ba(1)-S(3)#1		3.155(2)	2.276
Ba(1)- S(3)		3.2840(8)	
Ba(1)- S(3)#2		3.2840(8)	
Ba(1)- S(2)#3		3.3814(14)	
Ba(1)- S(2)#4		3.3837(15)	
Ba(1)- S(2)#5		3.3814(14)	
Ba(1)- S(2)#1		3.3837(15)	
Ba(1)-S(1)		3.153(2)	
Ba(1)- S(1)#6		3.201(2)	
Sb(1)- S(3)		2.375(2)	3.211
Sb(1)- S(2)#7		2.5199(14)	
Sb(1)- S(2)		2.5199(15)	3.073
S(2)- B(1)		1.816(5)	
S(1)- B(1)		1.756(9)	
Atom–Atom–Atom	**Angle [°]**	**Atom–Atom–Atom**	**Angle [°]**
S3–Sb1–S2	97.68(5)	S2#11–B1–S2	116.6(5)
S3–Sb1–S2#7	97.68(5)	S1–B1–S2	121.7(2)
S2–Sb1–S2#7	76.65(6)	S1–B1–S2#11	121.7(2)

Symmetry transformations used to generate equivalent atoms:#1 1-X, 1-Y, 1-Z; #2 +X, -1+Y, +Z; #3 1/2-X, -1/2+Y, -1/2+Z; #4 1-X, -1/2+Y, 1-Z; #5 1/2-X, 1-Y, -1/2+Z; #6 1/2+X, +Y, 1/2-Z; #7 +X, 3/2-Y, +Z. #11: +X, 0.5-Y, +Z.

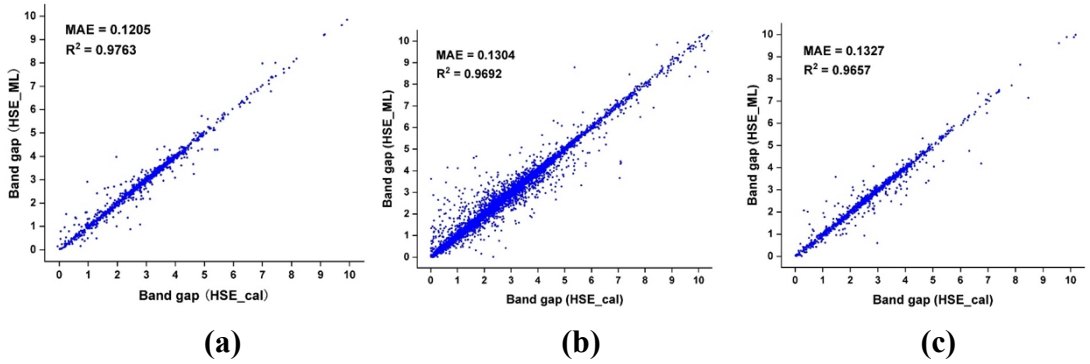

Figure S1. Prediction accuracy and fitting capability of our developed deep learning model for predicting HSE band gaps of crystals on the test data (a), training data (b) and validation data (c).

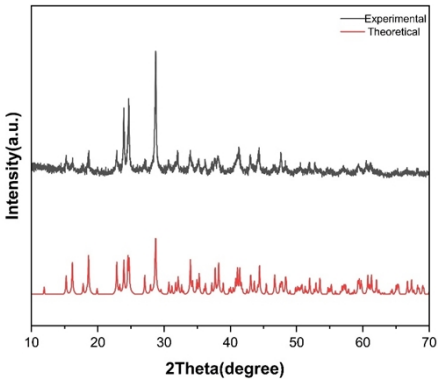

Figure S2. Simulated and measured powder X-ray diffraction patterns for $BaSbBS_4$.

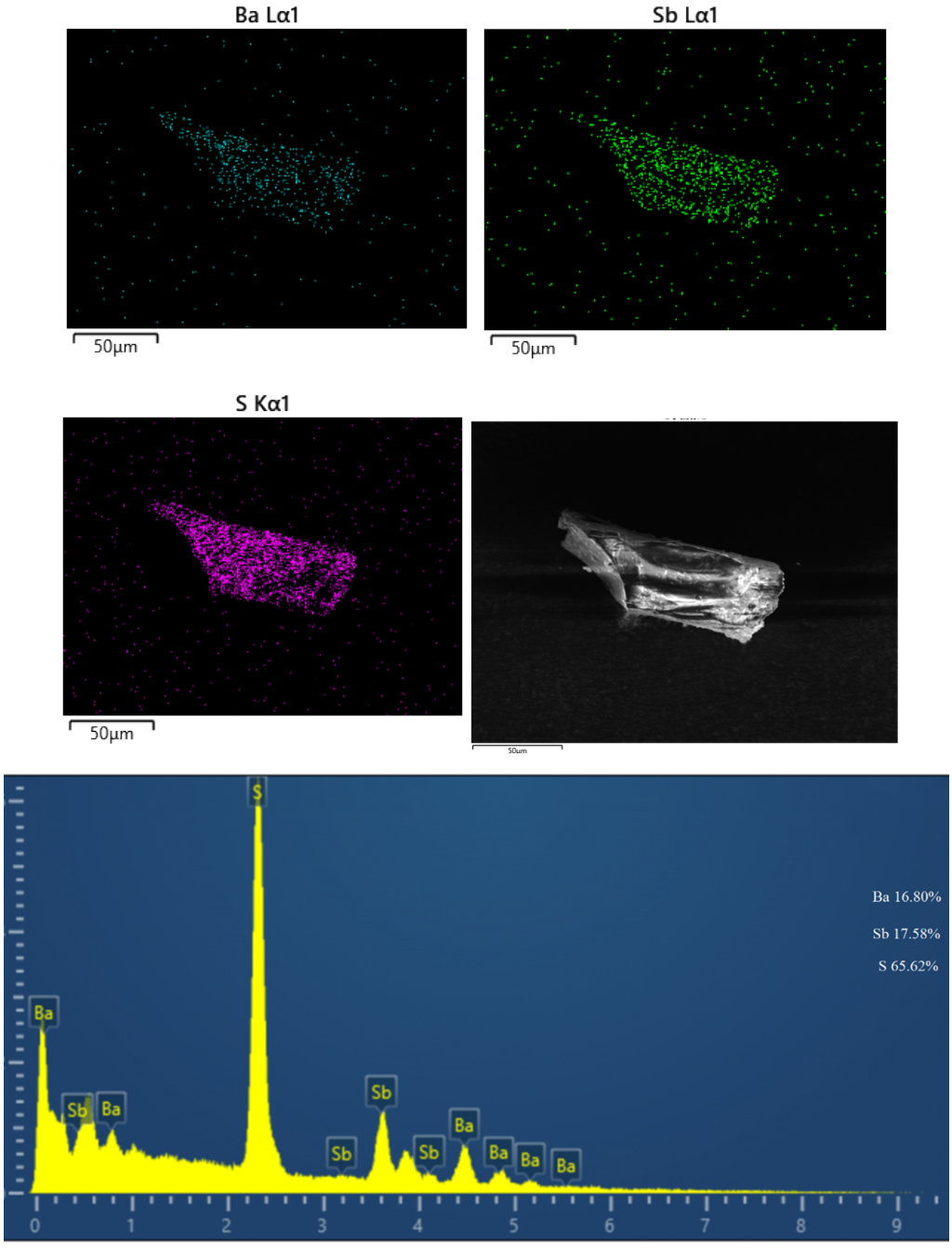

Figure S3. EDS maps of $BaSbBS_4$.

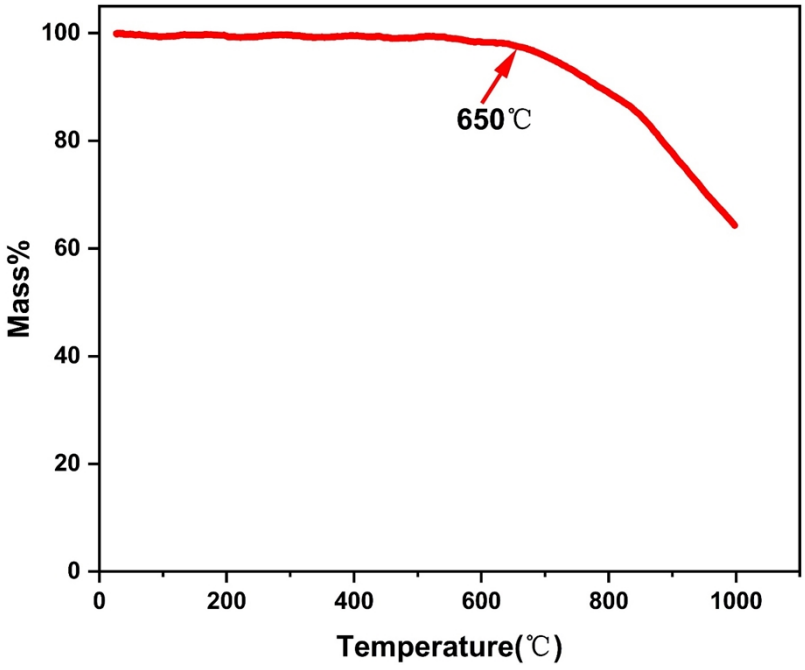

Figure S4. The TG (Thermogravimetry Analysis) for $BaSbBS_4$.

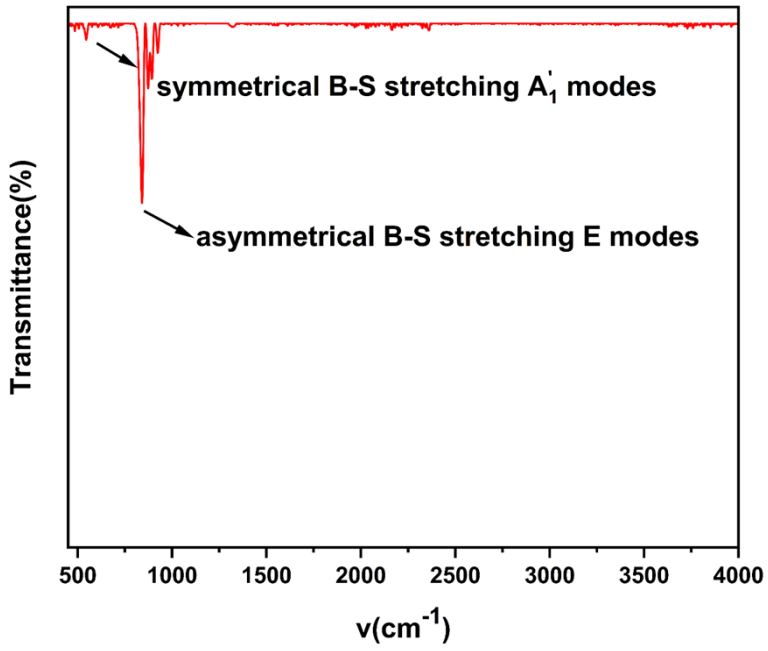

Figure S5. Infrared spectra for $BaSbBS_4$.

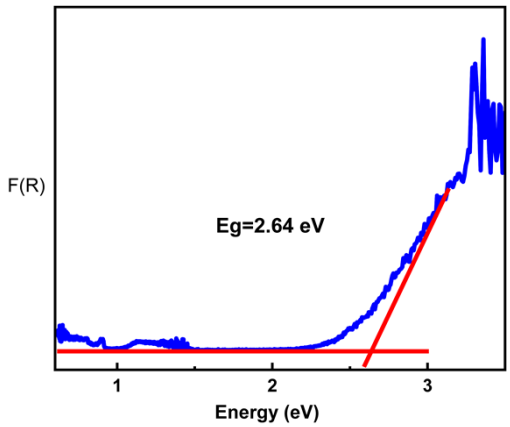

Figure S6. UV-vis spectra for $BaSbBS_4$.

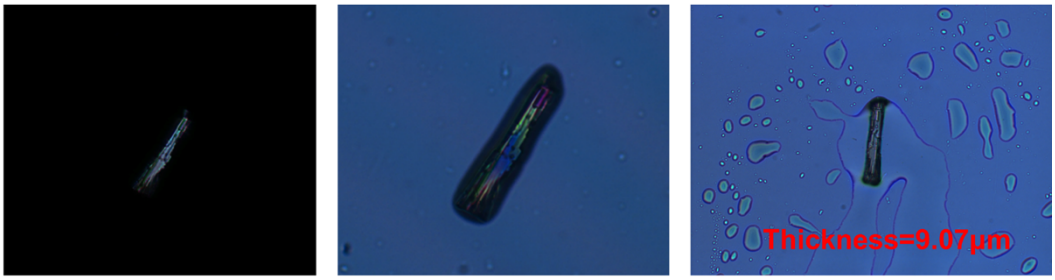

Figure S7. The crystal before compensation (a) and after compensation (b) with a tilting compensator under orthogonal polarizers. (c) Thickness of measured crystal.

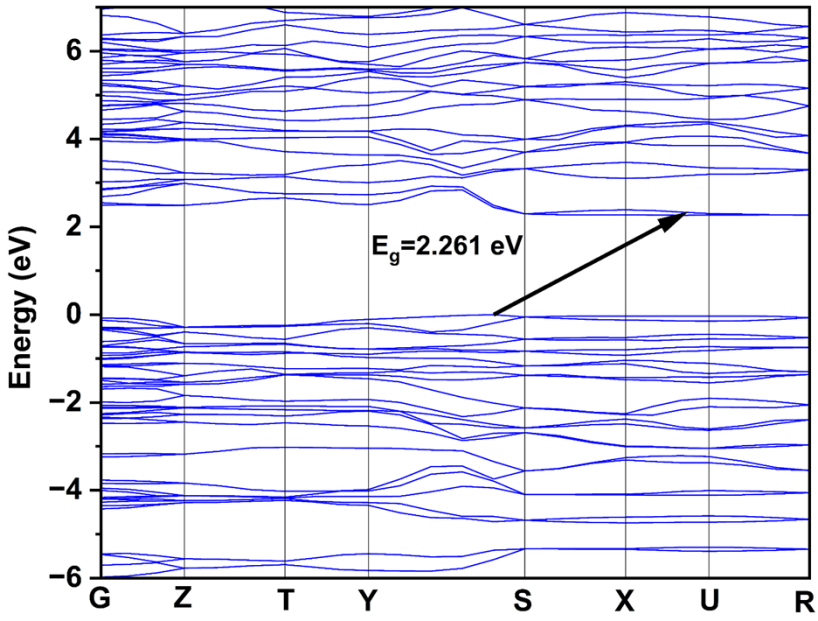

Figure S8. The calculated band structures for $BaSbBS_4$.

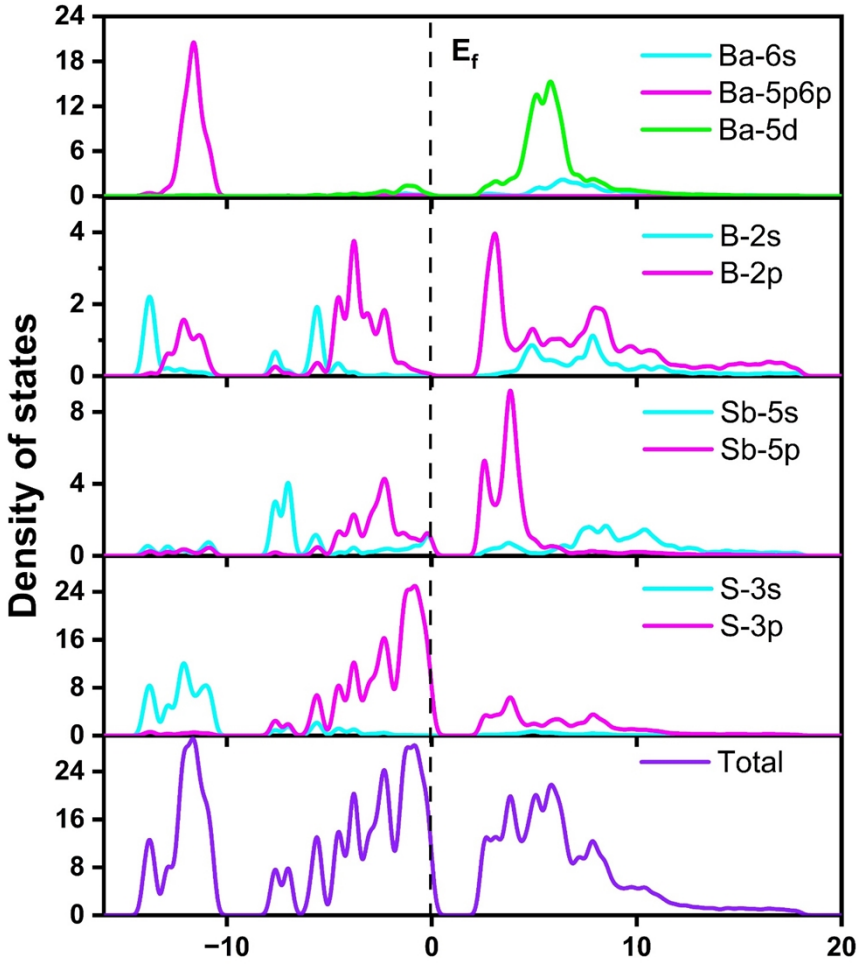

Figure S9. The partial density of state for $BaSbBS_4$.

References

1. T. Xie and J. C. Grossman, Crystal Graph Convolutional Neural Networks for an Accurate and Interpretable Prediction of Material Properties, *Phys. Rev. Lett.*, 2018, **120**, 145301.
2. C. Chen, W. Ye, Y. Zuo, C. Zheng and S. P. Ong, Graph Networks as a Universal Machine Learning Framework for Molecules and Crystals, *Chem. Mat.*, 2019, **31**, 3564-3572.
3. K. T. Schutt, H. E. Sauceda, P. J. Kindermans, A. Tkatchenko and K. R. Muller, SchNet - A deep learning architecture for molecules and materials, *J. Chem. Phys.*, 2018, **148**, 241722.
4. S. Kim, M. Lee, C. Hong, Y. Yoon, H. An, D. Lee, W. Jeong, D. Yoo, Y. Kang, Y. Youn and S. Han, A band-gap database for semiconducting inorganic materials calculated with hybrid functional, *Sci. Data*, 2020, **7**, 387.
5. A. Jain, S. P. Ong, G. Hautier, W. Chen, W. D. Richards, S. Dacek, S. Cholia, D. Gunter, D. Skinner, G. Ceder and K. A. Persson, Commentary: The Materials Project: A materials genome approach to accelerating materials innovation, *ALP Mater.*, 2013, **1**, 011002.
6. S. P. Ong, W. D. Richards, A. Jain, G. Hautier, M. Kocher, S. Cholia, D. Gunter, V. L. Chevrier, K. A. Persson and G. Ceder, Python Materials Genomics (pymatgen): A robust, open-source python library for materials analysis, *Comput. Mater. Sci.*, 2013, **68**, 314-319.
7. S. P. Ong, S. Cholia, A. Jain, M. Brafman, D. Gunter, G. Ceder and K. A. Persson, The Materials Application Programming Interface (API): A simple, flexible and efficient API for materials data based on REpresentational State Transfer (REST) principles, *Comput. Mater. Sci.*, 2015, **97**, 209-215.
8. V. Milman, B. Winkler, J. A. White, C. J. Pickard, M. C. Payne, E. V. Akhmatskaya and R. H. Nobes, Electronic structure, properties, and phase stability of inorganic crystals: A pseudopotential plane-wave study, *Int. J. Quantum Chem.*, 2000, **77**, 895-910.
9. M. D. Segall, P. J. D. Lindan, M. J. Probert, C. J. Pickard, P. J. Hasnip, S. J. Clark and M. C. Payne, First-principles simulation: ideas, illustrations and the CASTEP code, *J. Phys. Condens. Matter*, 2002, **14**, 2717-2744.
10. J. P. Perdew, K. Burke and M. Ernzerhof, Generalized Gradient Approximation Made Simple, *Phys. Rev. Lett.*, 1996, **77**, 3865-3868.
11. J. S. Lin, A. Qteish, M. C. Payne and V. V. Heine, Optimized and transferable nonlocal separable ab initio pseudopotentials, *Phys. Rev. B* 1993, **47**, 4174-4180.
12. F. Bassani, G. P. Parravicini, R. A. Ballinger and J. L. Birman, Electronic States and Optical Transitions in Solids, *Phys. Today*, 1976, **29**, 58-59.
13. C.-L. Hu, J. Chen, Z. Fang, R.-L. Tang and J.-G. Mao, LiB2O3F: A Beryllium-Free Deep-Ultraviolet Nonlinear Optical Material Designed Based on a Boron-Rich Strategy, *Chem. Mat.*, 2021, **33**, 4783-4791.
14. R. Blessing, An empirical correction for absorption anisotropy, *Acta Crystallogr. Sect. A*, 1995, **51**, 33-38.

15. G. M. Sheldrick, SHELXT - integrated space-group and crystal-structure determination, *Acta Crystallogr. A Found. Adv.*, 2015, **71**, 3-8.
16. A. L. Spek, Single-crystal structure validation with the programPLATON, *J. Appl. Crystallogr.*, 2003, **36**, 7-13.
17. R. Zhao, J. Zhou, X. Liu, R. Li and Q. Tang, A new solvothermal route to crystalline proustite Ag_3AsS_3 with photocatalytic properties, *Inorg. Chem. Commun.*, 2014, **46**, 17-20.
18. J. P. Rosenstingl, F., Neuberechnung der Kristallstruktur von natuerlichem und synthetischem monoklinen Ag_3AsS_3 (=Xanthokon) nebst einer Diskussion zur Symmetrie, *Mitt .Österr. Miner.Ges.* , 1993, **138**, 9-15.
19. Y. Guo, F. Liang, M. Zhou, Z. Lin, J. Yao and Y. Wu, $BaM_2As_2S_6$ (M = Cd, Hg): Synthesis, crystal structure, optical and electronic properties, *J. Alloys Compd.*, 2018, **762**, 143-148.
20. R. G. Iyer and M. G. Kanatzidis, Controlling Lewis basicity in polythioarsenate fluxes: stabilization of $KSnAsS_5$ and $K_2SnAs_2S_6$. Extended chains and slabs based on pyramidal β-$(AsS_4)^{3-}$ and $(AsS_3)^{3-}$ units, *Inorg. Chem.*, 2002, **41**, 3605-3607.
21. D. J. E. N. Mullen, W., Refinement of the crystal structures of realgar AsS and orpiment, As_2S_3, *Z. Kristallogr. Bd.*, 1972, **136**, 48-65.
22. A. R. Kampf, R. T. Downs, R. M. Housley, R. A. Jenkins and J. Hyršl, Anorpiment, As_2S_3, the triclinic dimorph of orpiment, *Mineral. Mag.*, 2018, **75**, 2857-2867.
23. A. Gavezzotti, F. Demartin, C. Castellano and I. Campostrini, Polymorphism of As_4S_3 (tris-(μ2-sulfido)-tetra-arsenic): accurate structure refinement on natural α- and β-dimorphites and inferred room temperature thermodynamic properties, *Phys. Chem. Miner.*, 2012, **40**, 175-182.
24. L. P. Bindi, V.; Bonazzi, P., Uzonite, As_4S_5, from the type locality: single-crystal, X-ray study and effects of exposure to light, *Can. Mineral.*, 2003, **41**, 1463-1468.
25. P. B. Bonazzi, L.; Popova, V.; Pratesi, G.; Menchetti, S., Alacranite, As_8S_9: structural study of the holotype and re-assignment of the original chemical formula, *Am. Miner.*, 2003, **88**, 1796-1800.
26. P. Schwarz, J. Wachter and M. Zabel, Novel Coordination Modes for E_4S_3 Cage Molecules (E = P, As) in Unprecedented Quaternary $As_4S_3(CuCl)_n$ (n = 1,2) Solid-State Phases, *Eur. J. Inorg. Chem.*, 2008, **2008**, 5460-5463.
27. I. Nakai and D. E. Appleman, Laffittite, $AgHgAsS_3$: crystal structure and second occurrence from the Getchell mine, Nevada, *Am. Miner.*, 1983, **68**, 235-244.
28. C. D. Morris, E. K. Qian, P. E. Meza, V. K. Sangwan, C. D. Malliakas, M. C. Hersam and M. G. Kanatzidis, Nanotube Structure of $AsPS_{(4-x)}Se_{(x)}$ (x = 0, 1), *Inorg. Chem.*, 2024, **63**, 4915-4924.
29. A. K. Iyer, J. B. Cho, M. J. Waters, J. S. Cho, B. M. Oxley, J. M. Rondinelli, J. I. Jang and M. G. Kanatzidis, Ba_2MAsQ_5 (Q = S and Se) Family of Polar Structures with Large Second Harmonic Generation and Phase Matchability, *Chem. Mat.*, 2022, **34**, 5283-5293.
30. R. Wang, X. Zhang, J. He, K. Bu, C. Zheng, J. Lin and F. Huang, Synthesis, Structure, and Optical Properties of Antiperovskite-Derived Ba_2MQ_3X (M = As, Sb; Q = S, Se; X = Cl, Br, I) Chalcohalides, *Inorg. Chem.*, 2018, **57**, 1449-1454.

31. W. S. Sheldrick and J. Kaub, Darstellung und Struktur von $Cs_2As_8S_{13}$, *Z. Naturforsch. B.*, 1985, **40**, 571-573.
32. Y. Sun, Y. Li, Y. Guo, Y. Liu, X. Cao, M. Ji, Z. You and Y. An, Solvothermal syntheses, crystal structures, and photoelectric response properties of two quaternary mercury-thioarsenates(III), *Inorg. Chem. Commun.*, 2021, **123**.
33. D. Yan, Y. Xiao, C. Liu, P. Hou, W. Chai, H. Hosono, H. Lin and Y. Liu, Two new members in the quaternary Cs-Ag-As-S family with different arrangements of Ag-S and As-S asymmetric building units: syntheses, structures, and theoretical studies, *Dalton. Trans.*, 2020, **49**, 9743-9750.
34. C. Liu, H. D. Yang, P. P. Hou, Y. Xiao, Y. Liu and H. Lin, $Cs_3CuAs_4Q_8$ (Q = S, Se): unique two-dimensional layered inorganic thioarsenates with the lowest Cu-to-As ratio and remarkable photocurrent responses, *Dalton. Trans.*, 2022, **51**, 904-909.
35. Y. Li, X. Cao, M. Ji, Z. You and Y. An, Solvothermal syntheses, structures, and characterizations of four thioarsenates $A_7Cu_4As_3S_{13}$ (A = Rb, Cs), $Rb_2Cu_5As_3S_8$, and $CsCu_2AsS_3$, *Inorg. Chem. Commun.*, 2022, **139**.
36. H. G. Yao, P. Zhou, S. H. Ji, R. C. Zhang, M. Ji, Y. L. An and G. L. Ning, Syntheses and characterization of a series of silver-thioantimonates(III) and thioarsenates(III) containing two types of silver-sulfur chains, *Inorg. Chem.*, 2010, **49**, 1186-1190.
37. L. Bindi, E. Makovicky, F. Nestola and L. De Battisti, Sinnerite, $Cu_6As_4S_9$, from the lengenbach quarry, binn valley, switzerland: description and re-investigation of the crystal structure, *Can. Mineral.*, 2013, **51**, 851-860.
38. J. H. Beck, S. and K. Koellisch, Hg_3AsE_4X (E= S, Se; X= Cl, Br, I), a family of isotypic compounds with an acentric, layered structure, *Inorg. Chem.*, 2000, **39**, 5847-5850.
39. D. Yan, P. Hou, C. Liu, W. Chai, X. Zheng, L. Zhang, M. Zhi, C. Zhou and Y. Liu, Effect of alkali cations on two-dimensional networks of two new quaternary thioarsenates (III) prepared by a facile surfactant-thermal method, *J. Solid State Chem.*, 2016, **241**, 47-53.
40. J. E. Jerome, P. T. Wood, W. T. Pennington and J. W. Kolis, Synthesis of New Low-Dimensional Quaternary Compounds, KCu_2AsS_3 and KCu_4AsS_4, in Supercritical Amine
Solvent. Alkali Metal Derivatives of Sulfosalt, *Inorg. Chem.*, 1994, **33**, 1733-1734.
41. S. Huber, C. Preitschaft, R. Weihrich and A. Pfitzner, Preparation, Crystal Structure, Electronic Structure, Impedance Spectroscopy, and Raman Spectroscopy of Li_3SbS_3 and Li_3AsS_3, *Z. Anorg. Allg. Chem.*, 2012, **638**, 2542-2548.
42. T. K. Bera, J. H. Song, A. J. Freeman, J. I. Jang, J. B. Ketterson and M. G. Kanatzidis, Soluble direct-band-gap semiconductors $LiAsS_2$ and $NaAsS_2$: large electronic structure effects from weak As···S interactions and strong nonlinear optical response, *Angew. Chem. Int. Ed.*, 2008, **47**, 7828-7832.
43. Y. Wu and W. Bensch, Synthesis, crystal structures, and optical properties of $NaCdPnS_3$ (Pn=As, Sb), *J. Alloys Compd.*, 2012, **511**, 35-40.
44. L. Bindi, A. Garavelli, D. Pinto, G. Pratesi and F. Vurro, Ordered distribution of I and Cl in the low-temperature crystal structure of mutnovskite, $Pb_4As_2S_6ICl$: An X-ray single-crystal study, *J. Solid State Chem.*, 2008, **181**, 306-312.

45. B. Ribar, C. Nicca and W. Nowacki, Dreidimensionale Verfeinerung der Kristallstruktur von Dufrenoysit, $Pb_8As_8S_{20}$, *Z. Kristallogr. Bd.*, 1969, **130**, 15-40.
46. B. J. Wuensch and W. Nowacki, The crystal structure of marrite, $PbAgAsS_3$, *Z. Kristallogr. Bd.*, 1967, **125**, 459-488.
47. C. Zhang, M. Ji, S. H. Ji and Y. L. An, Mild solvothermal syntheses and characterization of layered copper thioantimonates(III) and thioarsenate(III), *Inorg. Chem.*, 2014, **53**, 4856-4860.
48. Y. Li, X. Song, Y. Zhong, Y. Guo, M. Ji, Z. You and Y. An, Temperature controlling valance changes of crystalline thioarsenates and thioantimonates, *J. Alloys Compd.*, 2021, **872**.
49. H.-G. Yao, C.-F. Tang, Y.-L. An, Z.-J. Ou, G.-H. Wu, P. Lan and Y.-L. Zheng, Solvothermal syntheses and characterization of three new silver(I)/copper(I)-thioarsenates based on As^{2+}/As^{3+} ions, *J. Solid State Chem.*, 2017, **246**, 87-91.
50. C. Biagioni, L. Bindi, Y. Moëlo, C. J. Stanley and F. Zaccarini, Pyradoketosite, a new, unexpected, polymorph of Ag_3SbS_3 from the Monte Arsiccio mine (Apuan Alps, Tuscany, Italy), *Am. Miner.*, 2022, **107**, 1901-1909.
51. M. Oubakalla, M. Bouachri, K. Fareh, Y. Nejmi, M. E. Bouji, M. Aarab, M. Beraich, H. Majdoubi, M. Taibi, A. Bellaouchou, A. Zarrouk and M. Fahoume, The Ag_3SbS_3 thin film combining super-capacitive and absorptive behaviors: elaboration, characterization and DFT study, *Appl. Phys. A*, 2023, **130**.
52. C. Biagioni, F. Zaccarini, P. Roth and L. Bindi, Progress in the knowledge of 'ruby silvers': New structural and chemical data of pyrostilpnite, Ag_3SbS_3, *Mineral. Mag.*, 2020, **84**, 463-467.
53. L. Geng, Z.-Z. Luo and W.-D. Cheng, A new Sb-based polysulfide: $Ba_3Sb_2S_7$ containing $(S_2)^{2-}$ ligand, *J. Mol. Struct.*, 2013, **1048**, 482-486.
54. X. Wu, X. Gu, H. Pan, Y. Hu and K. Wu, Synthesis, Crystal Structures, Optical Properties and Theoretical Calculations of Two Metal Chalcogenides Ba_2AlSbS_5 and $Ba_2GaBiSe_5$, *Crystals*, 2018, **8**.
55. L. Geng, $Ba_2Sb_4GeS_{10}$, *Acta Crystallogr. Sect. E.-Crystallogr. Commun.*, 2013, **69**, i24.
56. C. Liu, Y. Shen, P. Hou, M. Zhi, C. Zhou, W. Chai, J. W. Cheng and Y. Liu, Hydrazine-hydrothermal synthesis and characterization of the two new quaternary thioantimonates(III) $BaAgSbS_3$ and $BaAgSbS_3{\cdot}H_2O$, *Inorg. Chem.*, 2015, **54**, 8931-8936.
57. G. Cordier, C. Schwidetzky and H. Schaefer, New SbS_2 strings in the $BaSb_2S_4$ structure, *J. Solid State Chem.*, 1984, **54**, 84-88.
58. W. Doerrscheidt and H. Schaefer, Zur Kenntnis des Bariumthioantimonats(III) $Ba_8Sb_6S_{17}$, *Z. Naturforsch.*, 1981, **36**, 410-414.
59. L. Wang, Y.-C. Hung, S.-J. Hwu, H.-J. Koo and W. Myunghwan, Synthesis, structure, and properties of a new family of mixed-framework chalcohalide semiconductors: $CdSbS_2X$ (X = Cl, Br), $CdBiS_2X$(X = Cl, Br), and $CdBiSe_2X$ (X = Br, I), *Chem. Mat.*, 2006, **18**, 1219-1225.
60. C. X. Du, F. Y. Qi, J. Chen and M. Baiyin, Two Mercury Antimony Chalcogenides $Cs_2HgSb_4S_8$ and $Cs_2Hg_2Sb_2Se_6$ with Cesium Cations as Counterions, *ACS Omega*,

2018, **3**, 15168-15173.
61. J. P. Yohannan and K. Vidyasagar, Syntheses and characterization of one-dimensional alkali metal antimony(III) thiostannates(IV), $A_2Sb_2Sn_3S_{10}$ (A=K, Rb, Cs), *J. Solid State Chem.*, 2015, **221**, 426-432.
62. G. Dittmar and H. Schaefer, Darstellung und Kristallstruktur von $Cs_2Sb_4S_7$, *Z. Anorg. Allg. Chem.*, 1978, **441**, 98-102.
63. N. Li, G. Teri, M. Shele, Sagala, Namila and M. Baiyin, The Solvothermal Synthesis and Properties of Thioantimonates Rb(1,4-DABH)Sb_4S_7 and $Cs_2ZnSb_2S_5$: 1D Anion Chains and 2D Anion Layer, *J. Cluster Sci.*, 2022, **34**, 1853-1860.
64. F.-Y. Qi, M. Shele and M. Baiyin, Two ternary antimony-chalcogenides of $Cs_4Sb_4S_8$ and $Cs_3Sb_5Se_9$, *Inorg. Chem. Commun.*, 2021, **129**.
65. W.-F. Chen, B.-W. Liu, S.-M. Pei, Q.-N. Yan, X.-M. Jiang and G.-C. Guo, ASb_5S_8 (A = K, Rb, and Cs): Thermal Switching of Infrared Nonlinear Optical Properties across the Crystal/Glass Transformation, *Chem. Mat.*, 2021, **33**, 3729-3735.
66. G. Yang, L. H. Li, C. Wu, M. G. Humphrey and C. Zhang, Ionothermal Synthesis of Metal Chalcogenides $M_2Ag_3Sb_3S_7$ (M = Rb, Cs) Displaying Nonlinear Optical Activity in the Infrared Region, *Inorg. Chem.*, 2019, **58**, 12582-12589.
67. F. Q. Huang and J. A. Ibers, Synthesis, structure, band gap, and electronic structure of $CsAgSb_4S_7$, *J. Solid State Chem.*, 2005, **178**, 212-217.
68. C. Liu, Y. Xiao, H. Wang, W. Chai, X. Liu, D. Yan, H. Lin and Y. Liu, One-Dimensional Chains in Pentanary Chalcogenides $A_2Ba_3Cu_2Sb_2S_{10}$(A = K, Rb, Cs) Displaying a Photocurrent Response, *Inorg. Chem.*, 2020, **59**, 1577-1581.
69. E. P. Spiridonov, L. Y. Krapiva, A. K. Gapeev, V. I. Stepanov, E. Y. Prushinskaya and V. Y. Volgin, Gruzdevite, $Cu_6Hg_3Sb_4S_{12}$ - a new mineral from the Chauvai antimony-mercury deposit, Central Asia, *Dokl. Akad. Nauk SSSR*, 1981, **261**, 971-976.
70. J. Qian, Y. Zhao, P. Zhao, H. Cheng, J. P. Hofmann and K. H. L. Zhang, Unraveling the electronic structure of $CuSbS_2$ thin film photocathodes for solar-driven hydrogen evolution, *Sci. China Mater.*, 2023, **66**, 3530-3538.
71. H. Yang, R. T. Downs, G. Costin and C. M. Eichler, The crystal structure of tvalchrelidzeite, Hg_3SbAsS_3, and a revison of its chemical formula, *Can. Mineral.*, 2007, **45**, 1529-1533.
72. W. Lei and H. Shiou-Jyh, A New Series of Chalcohalide Semiconductors with Composite $CdBr_2/Sb_2Se_3$ Lattices: Synthesis and Characterization of $CdSb_2Se_3Br_2$ and Indium Derivatives $InSb_2S_4X$ (X =Cl and Br) and InM_2Se_4Br (M=Sb and Bi), *Chem. Mat.*, 2007, **19**, 6212-6221.
73. M. Imafuku, I. Nakai and K. Nagashima, The crystal structure of a new synthetic sulfosalt, $KHgSbS_3$, *Mater. Res. Bull.*, 1986, **21**, 493-501.
74. R. Wang, X. Zhang, J. He, C. Zheng, J. Lin and F. Huang, Synthesis, crystal structure, electronic structure, and photoelectric response properties of KCu_2SbS_3, *Dalton. Trans.*, 2016, **45**, 3473-3479.
75. H.-G. Yao, M. Ji, S.-H. Ji, R.-C. Zhang, Y.-L. An and G.-l. Ning, Solvothermal Syntheses of Two Novel Layered Quaternary Silver−Antimony(III) Sulfides with Different Strategies, *Cryst. Growth Des.*, 2009, **9**, 3821-3824.
76. H. J. Zhao, P. F. Liu and L. M. Wu, Structural diversities in centrosymmetric

$La_8S_4Cl_8La_{12}S_8Cl_4[SbS_3]_8$and non-centrosymmetric $Ln_{12}S_8Cl_8[SbS_3]_4$ (Ln = La and Ce): syntheses, crystal and electronic structures, and optical properties, *Dalton. Trans.*, 2021, **50**, 2075-2082.
77. H. J. Zhao and L. J. Zhou, A Series of Noncentrosymmetric Antimony Sulfides $Ln_8Sb_2S_{15}$ (Ln = La, Pr, Nd) – Syntheses, Crystal and Electronic Structures, and NLO Properties, *Eur. J. Inorg. Chem.*, 2015, **2015**, 964-968.
78. D. Gout, S. Jobic, M. Evain and R. Brec, New Antimony Lanthanide Disulfide Dibromides $LnSbS_2Br_2$ (Ln=La, Ce): Crystal and Electronic Structures and Optical Properties, *J. Solid State Chem.*, 2001, **158**, 218-226.
79. H. Lin, Y.-Y. Li, M.-Y. Li, Z. Ma, L.-M. Wu, X.-T. Wu and Q.-L. Zhu, Centric-to-acentric structure transformation induced by a stereochemically active lone pair: a new insight for design of IR nonlinear optical materials, *J. Mater. Chem. C*, 2019, **7**, 4638-4643.
80. S. Huber and A. Pfitzner, The fourfold superstructure in $Li_3Sb_{11}S_{18}$, *Monatsh. Chem.*, 2018, **149**, 487-491.
81. A. Yalikun, K. Zhang, J. Han and Z. Yang, $LiSrSbS_3$: parallel configurations of lone pair electrons inducing a large birefringence, *Dalton. Trans.*, 2022, **51**, 14545-14550.
82. A. Abudurusuli, K. Wu, A. Tudi, Z. Yang and S. Pan, $ABaSbQ_3$(A = Li, Na; Q = S, Se): diverse arrangement modes of isolated SbQ_3 ligands regulating the magnitudes of birefringences, *Chem. Commun.*, 2019, **55**, 5143-5146.
83. J. E. Jerome, G. L. Schimek, G. W. Drake and J. W. Kolis, Synthesis, structure, and characterization of Na_2CuSbS_3, a new sulfosalt derivative from supercritical ethylenediamine, *Eur. J. Solid State Inorg. Chem.*, 1996, **33**, 765-782.
84. V. Manríquez, A. Galdámez and D. Ruiz-León, Preparation, crystal structure and characterization of α-$NaSbP_2S_6$ and β-$NaSbP_2S_6$ phases, *Mater. Res. Bull.*, 2006, **41**, 1337-1344.
85. G. Yang, C. Wu, J. Zhang and C. Zhang, Ionothermal Synthesis of Two New Thioantimonates with Transition Metal Regulation, *J. Cluster Sci.*, 2021, **33**, 1457-1465.
86. M. Shele, X. Tian and M. Baiyin, Solvothermal synthesis and properties of three antimony chalcogenides containing transition metal zinc, *J. Solid State Chem.*, 2021, **302**, 122401.
87. A. G. Vedeshwar, Optical Properties of Amorphous and Polycrystalline Stibnite(Sb_2S_3) Films, *J. Phys. III France* 1995, **5**, 1161-1172.
88. K. M. Koskela, B. C. Melot and R. L. Brutchey, Solution Deposition of a Bournonite $CuPbSbS_3$ Semiconductor Thin Film from the Dissolution of Bulk Materials with a Thiol-Amine Solvent Mixture, *J. Am. Chem. Soc.*, 2020, **142**, 6173-6179.
89. Q.-T. Xu, W.-D. Yao, X.-H. Li and S.-P. Guo, Investigation of the second-order nonlinear optical property of $Sr_6Sb_6S_{17}$, *J. Solid State Chem.*, 2021, **295**, 121915.
90. P. Wang, M. Abudoureheman, K. Zhang, J. Zheng, Z. Chen and Q. Wu, $Ag_4SnGe_2S_7$: A Noncentrosymmetric Chalcogenide in I_4-II-IV_2-VI_7 System with Non-Diamond-Like Structure Featuring $1D_\infty[SnGe_2S_8]^{6-}$ Infinite Chain, *Inorg. Chem.*, 2022,

61, 15303-15309.
91. S. del Bucchia, J. C. Jumas and M. Maurin, Etude du systeme SnS-BaS: Structure de $BaSn_2S_3$, *Acta Cryst. B*, 1980, **36**, 2935-2940.
92. W. D. C. B. Gunatilleke, A. F. May, A. R. H. Walker, A. J. Biacchi and G. S. Nolas, Synthesis, Crystal Structure, and Physical Properties of $BaSnS_2$, *Phys. Status Solidi RRL*, 2022, **16**, 2100624.
93. H. Yang, L. Pan, X. Wang, H. X. Deng, M. Zhong, Z. Zhou, Z. Lou, G. Shen and Z. Wei, Mixed-Valence-Driven Quasi-1D $Sn^{II}Sn^{IV}S_3$ with Highly Polarization-Sensitive UV–vis–NIR Photoresponse, *Adv. Funct. Mater.*, 2019, **29**, 1904416.
94. Z. H. Shi, Y. Chi, Z. D. Sun, W. Liu and S. P. Guo, $Sn_2Ga_2S_5$: A Type of IR Nonlinear-Optical Material, *Inorg. Chem.*, 2019, **58**, 12002-12006.
95. C. Li, Z. Lin, L. Kang, Z. Lin, H. Huang, J. Yao and Y. Wu, Sn_2SiS_4, synthesis, structure, optical and electronic properties, *Optical Materials*, 2015, **47**, 379-385.
96. P. P. K. Smith and B. G. Hyde, The homologous series $Sb_2S_3{\cdot}nPbS$: Structures of diantimony dilead pentasulphide, $Pb_2Sb_2S_5$, and the related phase diantimony ditin pentasulphide, $Sn_2Sb_2S_5$, *Acta Cryst. C*, 1983, **39**, 1498-1502.
97. S. S. Hegde, P. Murahari, B. J. Fernandes, R. Venkatesh and K. Ramesh, Synthesis, thermal stability and structural transition of cubic SnS nanoparticles, *J. Alloys Compd.*, 2020, **820**, 153116.
98. A. Kyono and M. Kimata, Crystal structures of chalcostibite ($CuSbS_2$) and emplectite ($CuBiS_2$): Structural relationship of stereochemical activity between chalcostibite and emplectite, *Am. Miner.*, 2005, **90**, 162-165.
99. E. Makovicky, The phase transformations and thermal expansion of the solid electrolyte Cu_3BiS_3 between 25 and 300°C, *J. Solid State Chem.*, 1983, **39**, 85-92.
100. J. Zhou, L. Wang, H. Wang, L. Luo, J. Li and F. Yu, $Ba_3(BS_3)(PS_4)$: the first alkaline-earth metal thioborate-thiophosphate with strong optical anisotropy originating from planar [BS_3] units, *Dalton. Trans.*, 2023, **52**, 16113-16117.
101. B. Krebs and H. U. Hürter, B_8S_{16}—An "Inorganic Porphine", *Angew. Chem. Int. Ed.*, 2003, **19**, 481-482.
102. Y. Kim and S. W. Martin*, Synthesis and Crystal Structure of Barium Thioborate $Ba_7(BS_3)_4S$, *Inorg. Chem. Commun.*, 2004, **43**, 2773-2775.
103. H. Li, G. Li, K. Wu, B. Zhang, Z. Yang and S. Pan, BaB_2S_4: An Efficient and Air-Stable Thioborate as Infrared Nonlinear Optical Material with High Laser Damage Threshold, *Chem. Mat.*, 2018, **30**, 7428-7432.
104. J. Kuchinke, J. Kueper and B. Krebs, Novel thioborates of cesium: Cs_3BS_3 and Li_2CsBS_3, *Z. Naturforsch. B.*, 2002, **57**, 1433-1438.
105. Y. Huang, Y. Zhang, D. Chu, Z. Yang, G. Li and S. Pan, HgB_2S_4: A d^{10} Metal Thioborate with Giant Birefringence and Wide Band Gap, *Chem. Mat.*, 2023, **35**, 4556-4563.
106. C. Püttmann, H. Diercks and B. Krebs, Synthesis, Crystal Structures and Properties of $M_3B_3S_6$(M = Na, K, Rb) And $LiSrB_3S_6$, *Phosphorus, Sulfur, and Silicon and the Related Elements*, 1992, **65**, 1-4.
107. J. Kuchinke, C. Jansen, A. Lindemann and B. Krebs, Syntheses and crystal

structures of the novel thioborates Na_3BS_3, K_3BS_3, and Rb_3BS_3, *Z. Anorg. Allg. Chem.*, 1950, **627**, 896-902.
108. L. S. Breton, G. Morrison, M. R. Lacroix, P. S. Halasyamani and H. C. Zur Loye, Lanthanide thioborates, an emerging class of nonlinear optical materials, efficiently synthesized using the boron-chalcogen mixture method, *Chem. Commun.*, 2022, **58**, 7992-7995.
109. P. Vinatier, P. Gravereau, M. Ménétrier, L. Trut and A. Levasseur, Li_3BS_3, *Acta Crys. C* 1994, **50**, 1180-1183.
110. F. Hiltmann and B. Krebs, $LiBaBS_3$ und $LiBaB_3S_6$: Zwei neue quaternare Thioborate mit trigonal-planar
koordiniertem Bor, *Z. Anorg. Allg. Chem.*, 1995, **621**, 424-430.
111. Y. Yun, W. Xie, Y. Huang, Z. Yang, K. Wu, G. Li and S. Pan, $NaBaBS_3$: A Promising Infrared Functional Material with Large Birefringence Induced by π-Conjugated [BS_3] Units, *Chem. Mat.*, 2022, **34**, 5215-5223.
112. F. Hiltmann, C. Jansen and B. Krebs, Li_3BS_3und $LiSrBS_3$: Neue Orthothioborate rnit trigonal-planar koordiniertem
Bor *Z. Anorg. Allg. Chem.*, 1996, **622**, 1508-1514.
113. A. Hammerschmidt, M. Doech, C. Puettmann and B. Krebs, $Sr_3(BS_3)_2$ und $Sr_3(B_3S_6)_2$: Zwei neue nicht-oxidische Chalkogenoborate mit trigonal-planar koordiniertem Bor, *Z. Anorg. Allg. Chem.*, 2003, **629**, 551-555.
114. Y. Yun, X. Hou, Z. Yang, G. Li and S. Pan, [$RbSr_3X$][$(BS_3)_2$] (X = Cl, Br): two salt-inclusion thioborates with large birefringence and structure transformation from centrosymmetric to asymmetric, *Chem. Commun.*, 2023, **60**, 118-121.
115. C. Jansen, J. Kueper and B. Krebs, $Na_2B_2S_5$ and $Li_2B_2S_5$: Two novel perthioborates with planar 1,2,4-trithia-3,5-diborolane rings, *Z. Anorg. Allg. Chem.*, 1995, **621**, 1322-1329.
116. Y. Y. Li, B. X. Li, G. Zhang, L. J. Zhou, H. Lin, J. N. Shen, C. Y. Zhang, L. Chen and L. M. Wu, Syntheses, Characterization, and Optical Properties of Centrosymmetric $Ba_3(BS_3)_{1.5}(MS_3)_{0.5}$ and Noncentrosymmetric $Ba_3(BQ_3)(SbQ_3)$, *Inorg. Chem.*, 2015, **54**, 4761-4767.
117. M. A. Khan, J. WANG , P. Liu, L. Chen， and Y. Li，, $Ba_{13}(BS_3)_6(SnS_6)$: Synthesis, Crystal Structure, Electronic Structure, and Optical Property, *Chinese J. Struct. Chem.*, 2017, **36**, 204-210.
118. L. Geng, W. D. Cheng, W. L. Zhang, C. S. Lin, H. Zhang, Y. Y. Li and Z. Z. He, $BaM(BS_3)S$ (M = Sb, Bi): two new thioborate compounds with one-dimensional polymeric chain structure, *Inorg. Chem.*, 2010, **49**, 6609-6615.
119. L. Geng, W. D. Cheng, W. L. Zhang, Y. Y. Li, Z. Z. Luo, H. Zhang, C. S. Lin and Z. Z. He, Syntheses, crystal structures and characterizations of two new quaternary thioborates: $PbMBS_4$ (M = Sb, Bi), *Dalton. Trans.*, 2011, **40**, 4474-4479.